Theory and measurements of harmonic generation in semiconductor superlattices with applications in the 100 GHz to 1 THz range

M. F. Pereira
Materials and Engineering Research Institute, Sheffield Hallam University, Howard Street, Sheffield S1 1WB, United Kingdom

J. P. Zubelli
Instituto de Matematica Pura e Aplicada, Rio de Janeiro 22460-320, Brazil

D. Winge and A. Wacker
Division of Mathematical Physics, Lunds Universitet, Box 118, 22100 Lund, Sweden

A. S. Rodrigues
Departamento de Física e Astronomia and Centro de Física de Porto, Universidade do Porto, 4169-007 Porto, Portugal

V. Anfertev and V. Vaks
Institute for Physics of Microstructures, RAS, Nizhny Novgorod, 603087, Russia
(Received 21 December 2016; revised manuscript received 11 June 2017; published 25 July 2017)

This manuscript describes harmonic generation in semiconductor superlattices, starting from a nonequilibrium Green's functions input to relaxation rate–type analytical approximations for the Boltzmann equation in which imperfections in the structure lead to asymmetric current flow and scattering processes under forward and reverse bias. The resulting current-voltage curves and the predicted consequences on harmonic generation, notably the development of even harmonics, are in good agreement with experiments. Significant output for frequencies close to 1 THz (7th harmonic) at room temperature, after excitation by a 141-GHz input signal, demonstrate the potential of superlattice devices for gigahertz to terahertz applications.

DOI: 10.1103/PhysRevB.96.045306

I. INTRODUCTION

Nonlinearities in semiconductor materials have been widely investigated and are well understood in the near-infrared and visible ranges, where powerful laser sources can be used to generate even strong nonresonant responses [1]. Large pulsed sources combined with nonlinear crystals have delivered pulsed, tunable GHz to THz sources [2–4]. In contrast, the GHz range still needs further progress towards efficient continuous-wave (CW), compact tunable powerful sources and predictive simulation tools to design new devices. At present, the main types of CW GHz and THz sources [5] are: electron-beam sources, such as gyrotrons, free electron lasers (FELs), and backward wave oscillators (BWOs); optically pumped far-infrared gas lasers; solid-state sources; frequency multipliers; THz quantum cascade lasers (QCLs); parametric sources; and photomixers. The key compact solid-state sources that can be designed as oscillators [6] to deliver input radiation above 300 GHz for mixers and multipliers are Schottky diodes, heterojunction barrier varactors, heterojunction bipolar transistors, high-electron-mobility transistors, resonant tunneling diodes, tunnel-injection transit-time devices, Gunn devices, and superlattice electron devices (SLEDs) [7], which are particularly high-performance fundamental sources in the 60–220 GHz range [8]. InP Gunn devices, from which second and third harmonics can also be extracted, have delivered 85 μW at 480 GHz [9,10]. THz QCLs may deliver the power and coherence for detection, but their wavelength tunability is extremely difficult and cryocooling is required. Furthermore, efficient devices have only been demonstrated for frequencies between 2 and 4 THz, while the realization of 1-THz QCL required magnetic fields of tens of teslas [11]. Recent photomixer concepts can reach this range, but emitted powers fall drastically with increasing frequency [12]. Difference frequency generation via resonant optical nonlinearities pumped by a mid-infrared (MIR) QCL [13] is a promising approach for on-chip simultaneous emission from the MIR to the THz range but would require GHz resonances, which are not easily achievable per design. Optical combs show strong promise for the MIR range [14], but their efficient coverage of the GHz to THz ranges is still to be demonstrated. Semiconductor superlattice (SSLs) can generate multiple harmonics from a GHz input and are more effective than Schottky diodes, which are the currently dominating technology for the GHz range. SSL multipliers have provided radiation up to 8.1 THz [15] and are the focus of this paper.

The principle underlying SSL multiplication [15] can be summarized as follows: perpendicular charge transport in biased superlattices is dominated by resonances due to the alignment of energy levels in different wells. These resonances yield various peaks in the current-voltage (I-V) characteristics connected with negative differential conductivity [16,17]. If the SSL is subjected to an external GHz–THz field, photon-assisted tunneling is possible and replica of the resonances are observed at biases which differ from alignment conditions by integer multiples of the photon energy [18,19], in good agreement between theory and measurements for weakly coupled superlattices [20]. Recent simulations, based on a phenomenological model, treating the SSL as an electronic circuit further illustrate the high-frequency response of charge

domains traveling through a strongly coupled semiconductor superlattice with an applied harmonic electromagnetic signal. The simple model shows that the SSL alone can amplify signals with a frequency close to the domain transient frequency and if the superlattice is connected to a resonator, amplification becomes possible for much higher frequencies of the external signal [21]. As a matter of fact, harmonic generation is a general feature of driven nonlinear systems, and Ref. [4] reports the observation of high-order harmonic generation (HHG) in a bulk crystal, together with a very simple model that shows how nonperturbative HHG could arise in a solid owing to periodically modulated Bloch oscillations. However, the model is purely qualitative, not predictive, and can only describe odd harmonics. In this paper we are not interested in circuit-equivalent approaches nor in phenomenological parameter fitting. Instead we focus on microscopic predictions of HHG in semiconductor superlattices, starting from nonequilibrium Green's functions (NEGF) methods [22–24]. Among the results presented here, we highlight:

(i) Nonsymmetric current-voltage curves are explained with a microscopic NEGF approach, which can be adjusted by a nonsymmetric generalization of the Tsu and Esaki [25] formula.

(ii) A predictive hybrid approach combining the NEGF input with a relaxation approximation to the Boltzmann equation for one miniband, complemented by an Ansatz solution for the asymmetric problem, describes HHG in good qualitative agreement with experiments for both odd and even harmonics.

The paper is organized as follows: We start with our mathematical model and then compare experiments with the simulations. A short summary follows. The interface roughness self-energy, which leads to asymmetric current flow in our NEGF calculations, is briefly revised in Appendix A. The figures are complemented by tables with numerical data in Appendix B.

II. THEORY

The nonlinear current density in a SSL with period d subjected simultaneously to a static bias $E_{dc}d$ and a field with amplitude E_{ac} oscillating at frequency ν, i.e., $E = E_{dc} + E_{ac}\cos(2\pi\nu t)$, can be cast as [26–28]

$$
\begin{aligned}
j &= j_{dc} + \sum_{l=-\infty}^{\infty} j_l^c \cos(2\pi\nu l t) + j_l^s \sin(2\pi l\nu t),\\
j_{dc} &= \sum_{p=-\infty}^{\infty} J_p^2(\alpha)\,\Upsilon(U),\\
j_l^c &= \sum_{p=-\infty}^{\infty} J_p(\alpha)\,(J_{p+l}(\alpha) + J_{p-l}(\alpha))\,\Upsilon(U),\\
j_l^s &= \sum_{p=-\infty}^{\infty} J_p(\alpha)\,(J_{p+l}(\alpha) - J_{p-l}(\alpha))\,K(U). \qquad (1)
\end{aligned}
$$

Here, J_l is the Bessel function of the first kind and order l and $U = u + ph\nu$, where $u = eE_{dc}d$ is the energy drop per period.

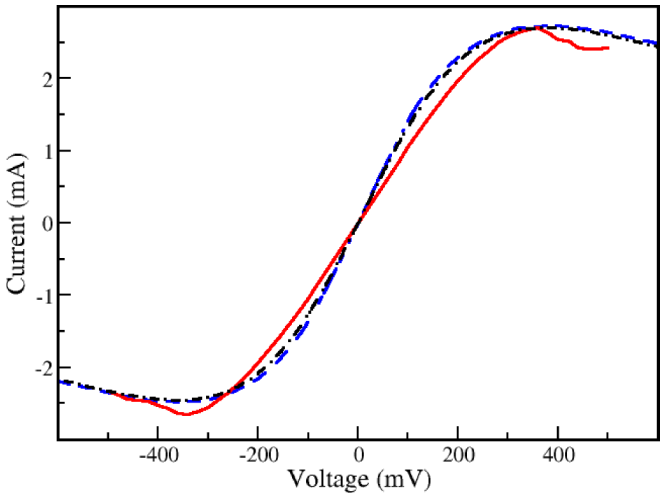

FIG. 1. Comparison of current-voltage curves calculated with the NEGF approach (black dashed), the fit to the hybrid approach formula (blue dot-dashed) of Eq. (3), and the experimental data (red solid). The contact area converting current density into current is 1.26×10^{-12} m^2.

Note that in Fig. 1 the total voltage $V = (u \times N_{\rm per})/e$ is shown. A very important parameter appears in Eq. (1), $\alpha = eE_{ac}d/h\nu$. The other parameters in the relaxation rate approximation [26–28] can be combined to express the functions Υ and K in a simple and useful format,

$$
\Upsilon(U) = 2j_0\frac{U/\Gamma}{1+(U/\Gamma)^2}, K(U) = \frac{2j_0}{1+(U/\Gamma)^2},
$$

$$
j_0 = \frac{2d|\mathcal{T}|/\hbar}{(2\pi)^3}\int_{-\pi/d}^{\pi/d} dq \int d^2k \cos(qd) n_F(k,q), \qquad (2)
$$

where $n_F(k,q)$ is the Fermi distribution to which the occupation function reduces to in the relaxation rate approximation, characterized by the scattering rate Γ. The expression for j_0 above stems from a simple model assuming a tight-binding dispersion and next-neighbor coupling $|\mathcal{T}|$. Note that in the static case ($\nu = 0$), the current density reduces exactly to the Tsu and Esaki expression [25], $j = j_{dc} = \Upsilon(U)$, where we have used $\sum_{p=-\infty}^{\infty} J_p^2(\alpha) = 1$. However, in real superlattices, the interface of GaAs over $Al_{1-x}Ga_xAs$ is worse than $Al_{1-x}Ga_xAs$ over GaAs, as repeated well and barrier regions are grown. The interface roughness self-energy and the parameters used to describe each interface are explained in Appendix A. Just this difference in interfaces, which is included in our NEGF calculations, makes it clear that the flow from right to left cannot be equal to that from left to right, as seen in the experiments of Fig. 1, which also shows that the full NEGF curve can be reproduced in excellent agreement, modifying the Tsu and Esaki limit,

$$
j_0 = \begin{cases} j_0^+ & U > 0 \\ j_0^- & U < 0 \end{cases}, \quad \Gamma = \begin{cases} \Gamma^+ & U > 0 \\ \Gamma^- & U < 0. \end{cases} \qquad (3)
$$

The key to understand our model is the fact that as seen experimentally [18–20], in a SSL under irradiation, photon-assisted tunneling generates a replica with peaks determined by $U = u + ph\nu$ in Eq. (1). Thus, this rectified energy drop

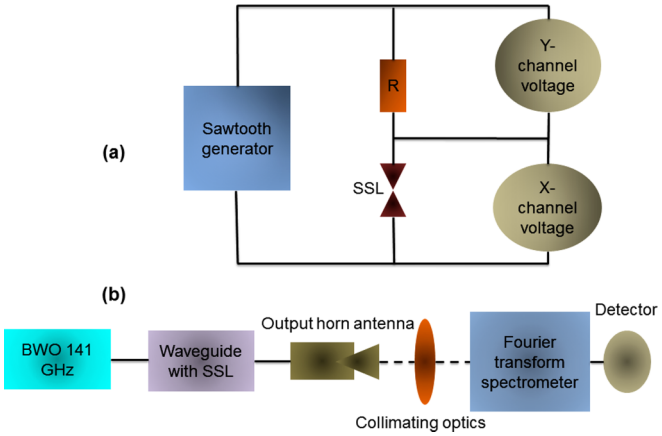

FIG. 2. Diagram of the experimental setup used to measure the current-voltage characteristics (a) and the harmonic power (b).

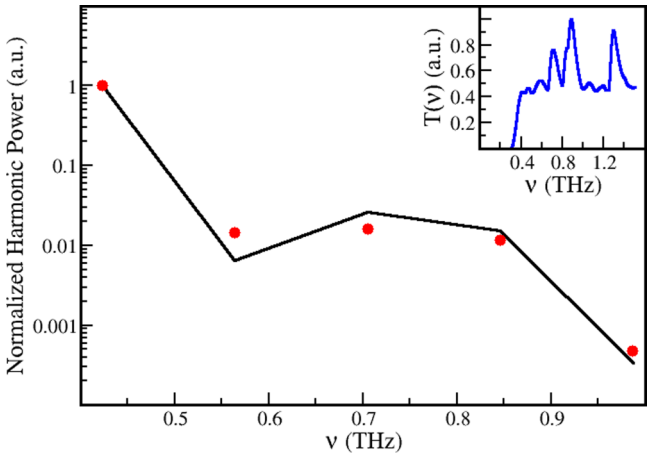

FIG. 3. Ratio of the emitted optical power for the nth harmonic to the 3rd harmonic nonlinearly generated by a field oscillating 141 GHz. The black solid line has been calculated using our theory and assuming an incident power of ~47 μW, or equivalently, $\alpha = 28.3$. From left to right, red circles are the corresponding experimental data for the third, fourth, fifth, sixth, and seventh harmonic. The inset shows the normalized transmission function of the waveguide structure where the superlattice is inserted.

per period is used in the ansatz equation (3). The resulting hybrid approach is predictive, since $j_0^{\pm}$ and $\Gamma^{\pm}$ are obtained per adjustment to the NEGF calculation.

Experimental teams without access to Boltzmann, NEGF, or Monte Carlo methods can fit the experimental I-V curve to extract these parameters, which can then be plugged into the analytical equations (1) and (2).

III. MEASUREMENTS AND SIMULATIONS

The experimental current-voltage curve, compared with our simulations in Fig. 1, was measured with an oscilloscope in XY mode (without time sweep). See the diagram in Fig. 2. Voltage from a sawtooth generator (frequency about 1 kHz) was applied to the SSL and load resistor which were connected in series. The circuit center point (connection of resistor, SSL diode, and X oscilloscope input) was isolated from the ground by means of a voltage follower. Thus the voltage from the SSL diode was displayed in the X axis of the oscilloscope. Another channel delivering voltage from load resistor R, which is proportional of current through the SSL, was displayed in the Y axis of the oscilloscope.

The SSL in the experiments has 18 periods of 6.23 nm each with 18 monolayers GaAs and four monolayers AlAs and was homogeneously doped with silicon. A temperature $T = 300$ K and an electron density of 1.5×10^{18} cm^{-3} have been used as input to the NEGF calculations [22,24]. The contact area used to compare the measured current and NEGF calculated current density is 1.26×10^{-12} m^2. These are similar but not identical to the values that we see, e.g., in Ref. [29], which has the same structure but nominally a slightly larger doping.

The exact NEGF calculations (black-dashed curve) and the combined Eqs. (1), (2), and (3) (blue-dot-dashed) results are essentially indistinguishable. Unexpected charge accumulation, traps, and defects make the problem even more asymmetric, but we do not have enough information about the sample to add these effects, which we attribute to the difference between the calculations and the experiments (red solid). The parameters extracted from the NEGF calculations and used in the ansatz solution are: $\Gamma^+, \Gamma^- = 21, 20$ meV, $j_0^+, j_0^- = 2.14, 1.94 \times 10^9$A/m^2. For a comparison, a direct fit to the experiments yields: $\Gamma^+, \Gamma^- = 20, 19$ meV, $j_0^+, j_0^- = 2.14, 2.10 \times 10^9$ A/m^2.

The SSL was placed in a waveguide chamber with waveguide flange of 2-mm wavelength range input (WR6, WR7 waveguide type, D band, 1.651×0.826 mm, UG-387/U input flange) and output horn antenna. The waveguide transmission factor T(ν), calculated with MICROWAVE OFFICE [30], is shown in the inset of Fig. 3. This blocks the input radiation from the backward wave oscillator (BWO) pump at 141 GHz from the output. The SSL harmonic power was measured with a Bruker IFS 125HR Fourier transform spectrometer with frequency resolution 0.01 cm^{-1} (300 MHz). A silicon He-cooled bolometer was used as receiver (with noise-equivalent power 3×10^{-13} W Hz$^{-0.5}$). Even though signatures were measured up to the 10th harmonic, the signal-to-noise ratio was reliable only up to 10^{-10} W at the detector for a quantitative analysis. That is why we only show results up to the 7th harmonic in Fig. 3. The measured intensity in the third harmonic $\mathcal{P}_3(\nu)$ has been estimated experimentally to be of the order of 0.33 μW and all other harmonics powers are measured relative to this value, see Appendix B. Note that the cutoff eliminates the second harmonic predicted by the theory. The average emitted power due to the lth harmonic is directly obtained from the Poynting vector $\mathcal{P}_l(\nu) = \langle |\mathcal{J}_l(\nu)|^2 \rangle$ T(ν), where $\langle |\mathcal{J}_l(\nu)|^2 \rangle = (j_l^s)^2 + (j_l^c)^2$ is the root-mean-square value of the lth component of the expansion of the induced current density in Eq. (1). There are a number of geometric factors that limit the power actually detected, and these cannot be realistically introduced in the theory. However, they are the same for each harmonic and thus the most accurate way to compare theory and experiment is to eliminate these unknown quantities by taking the ratio of harmonic powers of order (l) to the third harmonic, i.e., the harmonic power ratio $= \mathcal{P}_l(\nu)/\mathcal{P}_3(\nu)$, as shown in Fig. 3. Thus

only the normalized waveguide frequency response, shown in the inset of Fig. 3, is taken into account to compare and contrast measured and calculated values of harmonic power. There was no bias applied and for polarity-independent current, only odd harmonics would be foreseen theoretically. The even harmonics detected and predicted evolve from the fact that $j_0^+ \neq j_0^-$ and $\Gamma^+ \neq \Gamma^-$.

We consistently attribute the differences between detected and predicted values to the very same imperfections and possible local fields that lead to differences between theory and experiment for the I - V curves in Fig. 1. At this point it is very important to stress that the experimental setup does not allow us to determine the small fraction of the 4.1 mW delivered by the BWO at 141 GHz that actually reaches the SSL. We have thus determined α by means of a nonlinear least-squares curve-fitting algorithm based on the Levenberg-Marquardt method [31]. This leads to the $\alpha = 28.3$ value used in Fig. 3. Assuming that the source delivers a plane wave of amplitude E_{dc}, a vacuum characteristic impedance of $Z_0 = 377\,\Omega$, a spot size determined by the exposed surface of the SSL, $A = 112\,\text{nm} \times 2\,\mu\text{m}$, and the SSL period $d = 6.23$ nm, with input frequency ω in GHz, we obtain a direct connection between the input power P_{in} (in mW) and $\alpha = eE_{ac}d/h\nu$, $P_{\text{in}}(\text{mW}) = 2.941 \times 10^{-9}\nu^2\alpha^2$. Thus, for $\alpha = 28.34$ and $\nu = 141$ GHz, $P_{\text{in}} \approx 4.7\,\mu$W.

Figure 4 compares the asymmetric full solution with different $j_0^{\pm}$ and $\Gamma^{\pm}$ (solid-black) with a symmetric version with $j_0 \equiv j_0^- = j_0^+ = 2.14 \times 10^9 \text{A/m}^2$ and $\Gamma \equiv \Gamma^- = \Gamma^+ = 20$ meV. This shows that the full theory is crucial to explain the even harmonics but plays a small role for the odd harmonics, which would be the only ones present in a high-quality superlattice with the same scattering at both interfaces and no symmetry-breaking defects or internal fields. Tables I, II, and III in Appendix B complement the analysis.

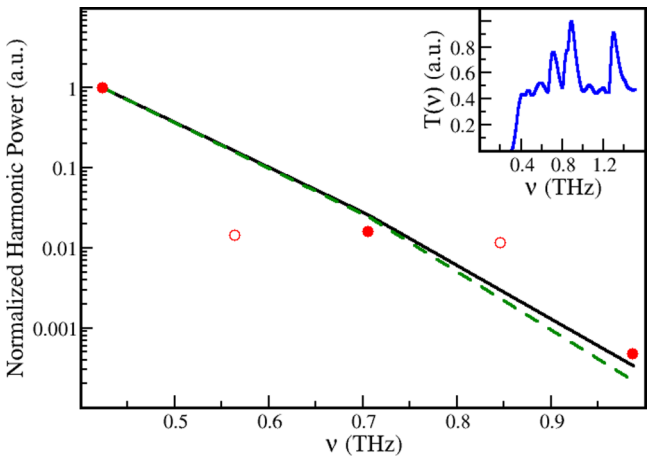

FIG. 4. Ratio of the emitted optical power for the nth harmonic to the 3rd harmonic nonlinearly generated by a field oscillating 141 GHz. Both curves have been calculated using $\alpha = 28.3$. The solid (black) curve is identical to the calculation in Fig. 3, except that only odd harmonics are shown for a direct comparison with the dashed (green) line, which has been computed with symmetric input parameters. From left to right, the red circles are the corresponding experimental data for the third, fourth, fifth, sixth, and seventh harmonic. The even harmonics are shown as open circles.

IV. CONCLUSION

In summary, the hybrid NEGF–relaxation rate approximation method presented in this paper leads to predictive simulations for the output power of semiconductor superlattices, in good qualitative agreement with experiments. The asymmetry in current-voltage directly reflects on both even and odd harmonics being predicted and detected. Combining the multipliers with superlattice electronic devices (SLEDs) that can deliver rf powers from 58 mW at 66 GHz to 15 mW at 108 GHz [8] can potentially lead to a new generation of compact and robust tunable solid-state sources for the GHz to THz range, covering a range that is not easily accessible for QCLs and other sources.

ACKNOWLEDGMENTS

The authors acknowledge support from European Cooperation in Science and Technology (COST) (MP1204, BM1205). The work of A.S.R. was partially funded by Fundação para a Ciência e a Tecnologia (UID/FIS/04650/2013).

APPENDIX A: INTERFACE ROUGHNESS SELF-ENERGY

In an actual structure, interface j may, instead of the real position z_j, be at $z_j + \xi_j(\mathbf{r})$, i.e., $\xi_j(\mathbf{r})$ is a thickness fluctuation with order of magnitude about one monolayer. We assume $\langle \xi_j(\mathbf{r}) \rangle = 0$ and

$$\langle \xi_i(\mathbf{r})\, \xi_j(\mathbf{r}') \rangle = \delta_{ij}\, \eta^2\, e^{-\frac{|\mathbf{r}-\mathbf{r}'|}{\lambda}} . \tag{A1}$$

Here η denotes the root-mean-square of the roughness height and λ characterizes a typical island size. The interface roughness potential is

$$V_{\alpha\beta}^{\text{rough}}(\mathbf{r}) = \sum_j \xi_j(\mathbf{r})\, \Delta E_j\, \psi_\alpha^*(z_j)\, \psi_\beta(z_j) . \tag{A2}$$

The corresponding self-energy in the second Born approximation is [22,24]

$$\begin{aligned} \Sigma^{\gtrless}_{\alpha\beta,\mathbf{k}}(E) &= \sum_{\alpha'\beta'} \int \frac{d^2\mathbf{k}'}{(2\pi)^2} \left\langle V^{\text{rough}}_{\alpha\alpha',\mathbf{k}-\mathbf{k}'}\, V^{\text{rough}}_{\beta'\beta,\mathbf{k}'-\mathbf{k}} \right\rangle G^{\gtrless}_{\alpha'\beta',\mathbf{k}'}(E) \\ &= \eta^2\, (\Delta E_j)^2 \sum_{\alpha'\beta',j} \int d^2\mathbf{r}\, e^{i(\mathbf{k}-\mathbf{k}')\mathbf{r}}\, e^{-\frac{r}{\lambda}}\, G^{\gtrless}_{\alpha'\beta',\mathbf{k}'}(E) \\ &\quad \times \psi_\alpha^*(z_j)\, \psi_{\alpha'}(z_j)\, \psi_\beta^*(z_j)\, \psi_\beta(z_j), \end{aligned} \tag{A3}$$

where $\psi_\alpha(z_j)$ is the wave function for Wannier state α at interface j and ΔE_j is the intersubband offset. For the AlAs over the GaAs interface we have used $\Delta E_j = -1$ eV, $\eta = 0.1$ nm, and $\lambda = 5$ nm and for the GaAs over AlAs interface $\Delta E_j = 1$ eV, $\eta = 0.2$ nm, and $\lambda = 5$ nm.

APPENDIX B: HARMONIC POWER TABLES

Tables I, II, and III complement Figs. 3 and 4. Table III summarizes the waveguide effect and explains why the predicted second harmonic is not detected, due to the waveguide cutoff. It depicts the harmonic powers comparing the calculated bare emitted power $\mathcal{P}_l^{\text{Bare}}(\nu) = \langle |\mathcal{J}_l(\nu)|^2 \rangle$, the full calculation, including the transmission through the waveguide

$\mathcal{P}_l(\nu) = \langle|\mathcal{J}_l(\nu)|^2\rangle\, \mathrm{T}(\nu)$, and the experiments. Furthermore "Experiment" denotes the normalized values $E_l(\nu)/E_3(\nu)$ and "Detected" gives the actually detected powers. $E_l(\nu)$ in Watts is also shown for reference. Even though higher harmonics were detected, the signal-to-noise ratio below 10^{-10} W does not allow for meaningful quantitative comparisons with the theory. Thus only results up to the 7th harmonic are shown. The table also shows how the predicted second harmonic is eliminated by the waveguide cutoff.

TABLE I. Normalized odd harmonic powers, experiment versus asymmetric full theory and the symmetric approximation.

Harmonic	Experiment	Full theory	Symmetric
3	1.00	1.00	1.00
5	1.6×10^{-2}	2.62×10^{-2}	2.50×10^{-2}
7	4.7×10^{-4}	3.35×10^{-4}	2.16×10^{-4}

TABLE II. Normalized even harmonic powers. Experiment versus asymmetric full theory and the symmetric approximation.

Harmonic	Experiment	Full theory	Symmetric
4	1.44×10^{-2}	6.50×10^{-3}	0
6	1.16×10^{-2}	1.54×10^{-2}	0.00

TABLE III. Waveguide effect.

Harmonic	ν (GHz)	$\mathcal{P}_l^{\mathrm{Bare}}(\nu)/\mathcal{P}_l^{Bare}(\nu)$	T(ν)	$\mathcal{P}_l(\nu)/\mathcal{P}_l(\nu)$	Experiment	Detected (W)
2	282	2.01×10^{-2}	0.00	0.00	0.00	0.00
3	423	1.00	0.43	1.00	1.00	3.30×10^{-7}
4	564	5.48×10^{-3}	0.51	6.50×10^{-3}	1.44×10^{-2}	4.75×10^{-9}
5	705	1.49×10^{-2}	0.76	2.62×10^{-2}	1.60×10^{-2}	5.28×10^{-9}
6	846	8.64×10^{-3}	0.77	1.54×10^{-2}	1.16×10^{-2}	3.83×10^{-9}
7	987	3.01×10^{-4}	0.47	3.35×10^{-4}	4.70×10^{-4}	1.55×10^{-10}

[1] M. Schaarschmidt and A. Knorr, J. Opt. Soc. Am. B **23**, 2342 (2006).
[2] W. Shi, Y. J. Ding, N. Fernelius, and K. Vodopyanov, Opt. Lett. **27**, 1454 (2002).
[3] S. Ya. Tochitsky, C. Sung, S. E. Trubnick, C. Joshi, and K. L. Vodopyanov, J. Opt. Soc. Am. B **24**, 2509 (2007).
[4] S. Ghimire, A. D. DiChiara, E. Sistrunk, P. Agostini, L. F. DiMauro, and D. A. Reis, Nat. Phys. **7**, 138 (2011).
[5] D. Saeedkia and S. Safavi-Naeini, J. Lightwave Technol. **26**, 2409 (2008).
[6] O. Momeni and E. Afshari, IEEE J. Solid State Circuits **46**, 583 (2011).
[7] H. Eisele, Electron. Lett. **46**, 8 (2010).
[8] H. Eisele, S. P. Khanna, and E. H. Linfield, Appl. Phys. Lett. **96**, 072101 (2010).
[9] H. Eisele, Electron. Lett. **46**, 422 (2010).
[10] H. Eisele, IEEE Microw. Compon. Lett. **19**, 416 (2009).
[11] G. Scalari, C. Walther, M. Fischer, R. Terazzi, H. Beere, D. Ritchie, and J. Faist, Laser Photonics Rev. **3**, 45 (2009).
[12] A. Rivera-Lavado, S. Preu, L. E. Garcia-Munoz, A. Generalov, J. Montero-de-Paz, G. Dohler, D. Lioubtchenko, M. Mendez-Aller, F. Sedlmeir, M. Schneidereit, H. G. L. Schwefel, S. Malzer, D. Segovia-Vargas, and A. V. Raisanen, IEEE Trans. Antennas Propag. **63**, 882 (2015).
[13] M. Razeghi, Q. Y. Lu, N. Bandyopadhyay, W. Zhou, D. Heydari, Y. Bai, and S. Slivken, Opt. Express **23**, 8462 (2015).
[14] J. Faist, G. Villares, G. Scalari, M. Roesch, C. Bonzon, A. Hugi, and M. Beck, Nanophotonics **5**, 272 (2016).
[15] V. Vaks, J. Infrared, Millimeter, Terahertz Waves **33**, 43 (2012).
[16] L. Esaki and L. L. Chang, Phys. Rev. Lett. **33**, 495 (1974).
[17] F. Capasso, K. Mohammed, and A. Y. Cho, Appl. Phys. Lett. **48**, 478 (1986).
[18] P. S. S. Guimaraes, B. J. Keay, Jann P. Kaminski, S. J. Allen, Jr., P. F. Hopkins, A. C. Gossard, L. T. Florez, and J. P. Harbison, Phys. Rev. Lett. **70**, 3792 (1993).
[19] B. J. Keay, S. J. Allen Jr., J. Galan, J. P. Kaminski, K. L. Campman, A. C. Gossard, U. Bhattacharya, and M. J. M. Rodwell, Phys. Rev. Lett. **75**, 4098 (1995).
[20] A. Wacker, A.-P. Jauho, S. Zeuner, and S. J. Allen, Phys. Rev. B **56**, 13268 (1997).
[21] V. V. Makarov, A. E. Hramov, A. A. Koronovskii, K. N. Alekseev, V. A. Maximenko, M. T. Greenaway, T. M. Fromhold, O. I. Moskalenko, and A. G. Balanov, Appl. Phys. Lett. **106**, 043503 (2015).
[22] T. Schmielau and M. F. Pereira, Jr., Appl. Phys. Lett. **95**, 231111 (2009).
[23] D. O. Winge, M. Lindskog, and A. Wacker, Opt. Express **22**, 18389 (2014).
[24] D. O. Winge, M. Franckie, C. Verdozzi, A. Wacker, and Mauro F. Pereira, J. Phys.: Conf. Ser. **696**, 012013 (2016).
[25] R. Tsu and L. Esaki, Appl. Phys. Lett. **22**, 562 (1973).
[26] A. Wacker, Phys. Rep. **357**, 1 (2002).
[27] A. A. Ignatov and Y. A. Romanov, Phys. Status Solidi B **7**, 3273 (1976).
[28] A. A. Ignatov, E. Schomburg, J. Grenzer, K. F. Renk, and E. P. Dodin, Z. Phys. B: Condens. Matter **98**, 187 (1995).
[29] F. Klappenberger, K. F. Renk, P. Renk, B. Rieder, Yu. I. Koshurinov, D. G. Pavelev, V. Ustinov, A. Zhukov, N. Maleev, and A. Vasilyev, Appl. Phys. Lett. **84**, 3924 (2004).
[30] MICROWAVE OFFICE: http://www.awrcorp.com/products/ni-awr-design-environment/microwave-office
[31] J. J. Moré, The Levenberg-Marquardt algorithm: Implementation and theory, in *Numerical Analysis*, edited by G. A. Watson, Lecture Notes in Mathematics Vol. 630 (Springer-Verlag, Berlin, 1977), pp. 105–116.